Complex resonant ice shelf vibrations

Luke G. Bennetts[1] and Michael H. Meylan[2]

[1]University of Adelaide, Adelaide, SA 5005, Australia

[2]University of Newcastle, Callaghan, NSW 2308, Australia

Abstract

The problem of ice-shelf vibrations forced by incident waves from the open ocean is considered, using a linear hydroelastic model involving combined thin-plate and potential-flow theories. Complex resonances are shown to generate near-resonant ice-shelf responses. An efficient algorithm is developed to capture the complex resonances, based on a homotopy, and initialised with the real-valued eigenfrequencies of a problem in which the ice shelf and sub-shelf water cavity are uncoupled from the open ocean. It is shown the complex resonances may be used to approximate the reflection coefficient in the frequency domain, and the large time ice-shelf response to an incident wave packet. Shelf thickening is shown to have a major effect on complex resonances at mid-range frequencies, resulting in difficulty exciting certain near-resonances in transient problems.

1 Introduction

Seismic measurements show that ice shelves vibrate in response to ocean waves over a wide frequency range, from swell to tsunami waves [18, 6, 4]. The phenomenon of wave-induced ice-shelf vibrations has been brought into focus by evidence of wave-induced calving of large icebergs [5], rift propagation [17], icequake activity [8], and triggering of catastrophic disintegration [20]. In a recent study of particular relevance, Chen et al. [8] correlate ice shelf vibration measurements with ocean wave measurements. They report large shelf vibrations in response to incident swell, infragravity and tsunami waves, but note associated shelf strains decrease with decreasing frequency, so the largest strains occur in the swell and infragraity regimes, with a peak at the high-frequency end of the infragravity regime. This informs a frequency range of interest for the present investigation covering high-frequency infragravity to low-frequency swell waves.

Mathematical models of wave-induced ice-shelf vibrations typically use linear thin-plate theory for the ice shelf and linear shallow-water or finite-depth potential-flow theory for the ocean, based on the early work of [12]. The shallow-water approximation creates a more tractable and easily calculable problem, but is valid only for long waves, roughly in the infragravity–tsunami regime, and can be highly inaccurate in the swell regime when compared to the finite-depth model [14]. The majority of models assume uniformity in one horizontal dimension, treat the ice shelf as clamped at the grounding line (the point at which the shelf no longer floats), and consider the problem in the frequency domain.

Particular attention has been given to predictions of near-resonant ice-shelf responses to incident waves from the open ocean, i.e. large peaks in maximum displacements at certain frequencies [33, 23, 16, 30]. An infinite sequence of near resonances exists, with each near resonance caused by the excitation of a particular natural mode of ice-shelf vibration [27]. The resonant behaviours have been associated to eigenproblems in which the ice shelf and sub-shelf cavity are uncoupled from the open ocean, and motions are trapped by imposing either a no-flux (Neumann) [33, 23] or no-pressure (Dirichlet) [30] condition at the open ocean end of the cavity. Papathanasiou et al. [30] observe in their numerical results, using the shallow-water approximation, that no-pressure eigenfrequencies approximate near-resonant peaks of the maximum shelf displacement better than the no-flux eigenfrequencies, but offer no reasoning.
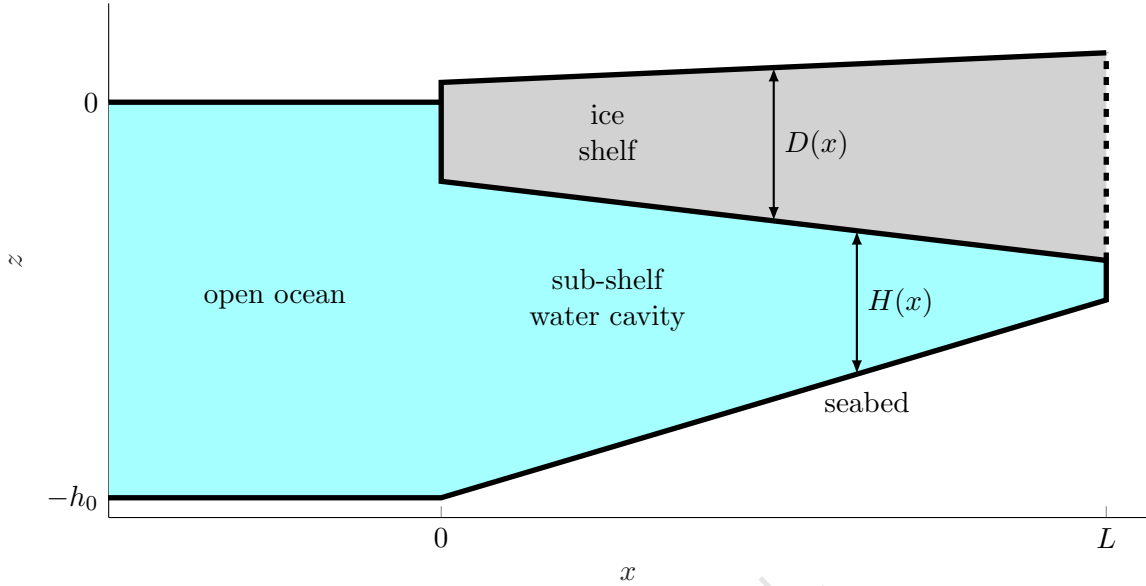
Figure 1: Schematic of the geometry (not to scale).

Most studies of near resonance model the ice shelf as having constant thickness and the seabed as flat, so that waves propagate unhindered through the shelf/cavity region. Exceptions are Ilyas et al. [13], who use a finite-element method in the sub-shelf water cavity that permits spatial seabed variations, and Meylan et al. [27], who combine the finite-element method with an expansion of the shelf vibrations in the natural modes of vibration to allow for both seabed variations and shelf thickness variations (as in Fig. 1). Meylan et al. [27] show shelf thickening towards the grounding line downshifts near-resonant frequencies (in comparison to a uniform shelf of the same mean thickness), and seabed shoaling beneath the shelf upshifts near-resonant frequencies. Numerical methods that accommodate shelf thickness and seabed variations have also been used [31, 34], but only for a handful of simulations, presumably due to the computational costs involved.

Near-resonant phenomena have been reported in other water-wave problems, such as wave interactions with bathymetric variations [7], and fixed, submerged and floating structures [19, 9, 21]. In these cognate problems, near resonances (and associated near trapping) have been attributed to full resonances (i.e. infinite responses) that exist when the governing equations are analytically extended into complex-frequency space, and are hence known as complex resonances. Complex resonances occur at complex-valued frequencies (often known as scattering frequencies [10]) with small imaginary parts and close to the real-valued near-resonant frequencies. Calculating complex resonances, i.e. the complex-resonant frequencies and associated eigenfunctions, generally involves a costly search of complex-frequency space around the near-resonant frequencies. Once found, they can be used in the singularity expansion method [11, 22, 25] to approximate solutions of transient problems at large times, giving information on near-resonance decay rates.

In this paper, complex resonances are shown to generate the near-resonant behaviour of ice shelves. An approximation of the vertical water motion is employed, which leads to a governing system of comparable structure to the shallow-water approximation, but is shown to be accurate over a much wider frequency range, similar to [2] for a sea-ice application. A step approximation is used to solve for problems involving variable geometry, and it is shown that frequency-domain solutions for ice shelves of hundreds of kilometres in length can be obtained in approximately one second. Near resonances are shown to bounded above and below by no-flux and no-pressure eigenfrequencies, respectively, and to tend towards no-pressure eigenfrequencies as frequency increases. The latter behaviour is explained in terms of the magnitude of a single coefficient that appears in the resonance condition for the coupled

2

problem. A homotopy is developed between the uncoupled eigenproblems and the ocean-coupled resonance problem. The homotopy is used to generate an efficient algorithm to calculate the complex resonances. It is shown that the complex resonances can be used to capture ice-shelf responses to incident wave packets at large times, via the singularity expansion method. Further, the complex-resonant frequencies are used to approximate the reflection coefficient in the frequency domain via a Blaschke product, which is a less well known application [26]. Ice-shelf thickening is shown to have a major impact on complex resonances in the mid-frequency range, and this is shown to make it difficult to excite certain resonances with incident wave packets.

2 Preliminaries

Consider the problem shown in Fig. 1, in which locations are defined by the Cartesian coordinates x in the horizontal direction and z in the vertical direction. An ice shelf of length L and thickness $D(x) \ll L$ has its front end located at $x = 0$. The sub-shelf water cavity has equilibrium depth $H(x) = h(x) - d(x)$, where $z = -h(x)$ and $z = -d(x)$ are the locations of the fixed, impermeable seabed and undisturbed ice shelf underside, respectively. In motion, the vibrating ice shelf underside is $z = -d(x) + w(x,t)$. The shelf and sub-shelf cavity are connected to the open ocean, which occupies $x < 0$, and in which the free surface is $z = u(x,t)$ and seabed is assumed flat and located at $z = -h_0$. The seabed is assumed to be continuous, so that $h(0) = h_0$.

The shelf is modelled as a thin elastic plate, with density $\rho_{\mathrm{i}} = 917 \, \mathrm{kg \, m^{-3}}$ and flexural rigidity $F(x) = E \, D^3 / 12 \, (1 - \nu^2)$, where $E = 11 \, \mathrm{GPa}$ is Young's modulus and $\nu = 0.3$ is Poisson's ratio. The water (both in the sub-shelf cavity and open ocean) is assumed homogeneous, with density $\rho_{\mathrm{w}} = 1025 \, \mathrm{kg \, m^{-3}}$. Water motion is modelled using potential-flow theory (i.e. inviscid, incompressible, irrotational motion), so that its velocity field is defined as the gradient of a scalar velocity potential $\Phi(x, z, t)$.

Linear motions are assumed, i.e. $|u|, |w| \ll \ell$, where ℓ is a characteristic horizontal length. Time-harmonic motions at a prescribed angular frequency ω are imposed via

$$\Phi(x, z, t) = \mathrm{Re} \left\{ \frac{g}{\mathrm{i}\,\omega} \, \phi(x, z) \, \mathrm{e}^{-\mathrm{i}\,\omega\,t} \right\}, \tag{1a}$$

$$u(x, t) = \mathrm{Re} \left\{ \eta(x) \, \mathrm{e}^{-\mathrm{i}\,\omega\,t} \right\} \quad \text{and} \quad w(x, t) = \mathrm{Re} \left\{ \zeta(x) \, \mathrm{e}^{-\mathrm{i}\,\omega\,t} \right\}, \tag{1b}$$

where ϕ, η and ζ are complex-valued functions, and $g = 9.81 \, \mathrm{m \, s^{-2}}$ is the constant of gravitational acceleration. Under the assumption of mild geometrical slopes, the vertical dependence of the velocity potential is approximated by the mode that supports propagating waves (in a local sense where the geometry varies), so that

$$\phi(x, z) \approx \varphi_0(x) \, Z_0(z) \quad \text{for} \quad x < 0, \quad \text{where} \quad Z_0 = \frac{\cosh k(z + h_0)}{\cosh(k \, h_0)}, \tag{2a}$$

$$\text{and} \quad \phi(x, z) \approx \varphi(x) \, Z(x, z) \quad \text{for} \quad 0 < x < L, \quad \text{where} \quad Z = \frac{\cosh \kappa(z + h)}{\cosh(\kappa \, H)}, \tag{2b}$$

with η and ζ approximated indirectly, and where $\eta = \varphi_0$ due to the uniform geometry (i.e. flat seabed) in the open water region ($x < 0$). The wavenumbers introduced in (2) are $k(\omega)$ in the open ocean ($x < 0$) and $\kappa(\omega : x)$ in the shelf/cavity ($0 < x < L$), which are the positive real roots of the dispersion relations

$$k \tanh(k \, h_0) = \sigma \quad \text{and} \quad (1 - \sigma \, d + \Gamma \, \kappa^4) \, \kappa \, \tanh(\kappa \, H) = \sigma, \tag{3}$$

where $\sigma = \omega^2 / g$ is a frequency parameter and $\Gamma = F / (\rho_{\mathrm{w}} \, g)$ is a scaled flexural rigidity.

3

The governing equations of the single-mode approximation in the shelf/cavity interval are

$$\left(a\,\varphi'\right)' + b\,\varphi + \sigma\,\zeta = 0 \quad \text{and} \quad (1 - \sigma\,d)\,\zeta + \mathcal{L}\{\zeta\} - \varphi = 0 \quad (0 < x < L), \tag{4}$$

where primes denote differentiation with respect to x, and $\mathcal{L}\{\zeta\} \equiv (\Gamma\,\zeta'')'' + (1 - \nu)\,\Gamma''\,\zeta''$. The coefficients $a(x)$ and $b(x)$ are

$$a = \int_{-h}^{-d} Z^2\,\mathrm{d}z \quad \text{and} \quad b = \kappa^2\,a - \kappa\,\tanh(\kappa\,H) + \frac{\mathrm{d}}{\mathrm{d}x}\int_{-h}^{-d} Z\,\frac{\mathrm{d}Z}{\mathrm{d}x}\,\mathrm{d}z - \int_{-h}^{-d}\left(\frac{\mathrm{d}Z}{\mathrm{d}x}\right)^2\,\mathrm{d}z. \tag{5}$$

The following boundary conditions are applied to (4):

$$\zeta''(0) = \zeta'''(0) = 0, \quad \zeta(L) = \zeta'(L) = 0 \quad \text{and} \quad \varphi'(L) = 0. \tag{6}$$

The first component of (6) imposes free-end conditions at the shelf front, i.e. vanishing of bending moment and shear stress. The bending-moment condition is an approximation, as water imposes a bending moment on the submerged portion of the shelf front. However, [15] provide numerical evidence the shelf-front bending moment has only a small influence on resonant responses. The second component of (6) clamps the shelf at its landward end, and the third component is no-flow through the vertical portion of the seabed at the grounding line.

The (reduced) velocity potential in the open water, φ_0, is expressed as

$$\varphi_0(x) = A_+\,\mathrm{e}^{\mathrm{i}\,k\,x} + A_-\,\mathrm{e}^{-\mathrm{i}\,k\,x} \quad (x < 0), \tag{7}$$

where the first component on the right-hand side is an incident wave with prescribed amplitude A_+, and the second component is a reflected wave with amplitude A_- to be found as part of the solution process. It is coupled to the (reduced) velocity potential in the shelf/cavity region, φ, by the jump conditions

$$v_0\,\varphi_0(0) = v\,\varphi(0) \quad \text{and} \quad a_0\,\varphi_0'(0)\,/\,v_0 = \left\{a\,\varphi'(0) + j\,\varphi(0)\right\}\,/\,v, \tag{8}$$

with coefficients

$$a_0 = \int_{-h_0}^{0} Z_0^2\,\mathrm{d}z, \quad v_0 = \int_{-h_0}^{-d(0)} Z_0\,\mathrm{d}z, \tag{9a}$$

$$v = \int_{-h_0}^{-d(0)} [Z]_{x=0}\,\mathrm{d}z \quad \text{and} \quad j = \int_{-h_0}^{-d(0)} \left[Z\,\frac{\mathrm{d}Z}{\mathrm{d}x}\right]_{x=0}\,\mathrm{d}z. \tag{9b}$$

The jump conditions are weak versions of continuity of pressure and horizontal velocity, respectively.

For a uniform shelf/cavity geometry, i.e. a shelf of constant thickness D over a flat seabed $h = h_0$, the velocity potential and shelf displacement are expressed as a sum of rightward $(+)$ and leftward $(-)$ propagating/decaying components, respectively,

$$\varphi(x) = \varphi_+(x) + \varphi_-(x - L) \quad \text{and} \quad \zeta(x) = \zeta_+(x) + \zeta_-(x - L) \quad (0 < x < L), \tag{10}$$

where

$$\varphi_\pm(x) = B_{0\pm}\,\mathrm{e}^{\pm\mathrm{i}\,\kappa\,x} - \frac{\Gamma}{a}\sum_{m=1,2}(\kappa^2 + \mu_m^2)\,\kappa\,\tanh(\kappa\,H)\,B_{m\pm}\,\mathrm{e}^{\pm\mathrm{i}\,\mu_m\,x}, \tag{11a}$$

$$\text{and} \quad \zeta_\pm(x) = \frac{\kappa\,\tanh(\kappa\,H)}{\sigma}B_{0\pm}\,\mathrm{e}^{\pm\mathrm{i}\,\kappa\,x} + \sum_{m=1,2}B_{m\pm}\,\mathrm{e}^{\pm\mathrm{i}\,\mu_m\,x}. \tag{11b}$$

In (11), μ_m $(m = 1, 2)$ are wavenumbers derived from the single-mode approximation, which typically have the properties $\mu_1 \in \mathbb{R}_+ + \mathrm{i}\,\mathbb{R}_+$ and $\mu_2 = -\overline{\mu_1}$, and $B_{m\pm}$ $(m = 0, 1, 2)$ are amplitudes to be determined.

The single-mode approximation (2) can be extended to a multi-mode approximation that captures the full-linear solution to any desired accuracy (in the absence of machine error; [1]). For piece-wise uniform geometry, the multi-mode approximation results in expressions similar to (7) and (10), but including evanescent waves, which are generated at the shelf front and grounding line, and allow the continuities of pressure and horizontal velocity to be satisfied throughout the water column at $x = 0$. Fig. 2(a) shows the single-mode and multi-mode approximations of $\mathrm{Re}(R)$ versus ω / π, where $R = A_- / A_+$ is the reflection coefficient, for a $D = 200\,\mathrm{m}$ thick shelf over a flat seabed at $h = h_0 = 300\,\mathrm{m}$. Ten modes are used for the multi-mode approximation, which is taken to be the full-linear solution. The approximation given by the shallow-water approximation is also shown. The piece-wise uniform geometry of the test problem gives a sufficient comparison of the approximations, as the shelf front is a strong scattering source.

The single-mode approximation is almost identical to the multi-mode approximation in the frequency range of interest, $0.01 \leq \omega / \pi \leq 0.04\,\mathrm{Hz}$. The frequency range shown extends up to $\omega / \pi = 0.1\,\mathrm{Hz}$ to show the slight inaccuracies in the single-mode approximation for higher frequencies, most notably the small frequency upshifting of the sharp minima. In contrast, inaccuracies are evident in the shallow-water approximation as low as $\omega / \pi \approx 0.02\,\mathrm{Hz}$. The inaccuracies grow with increasing frequency, and the shallow-water approximation has markedly different behaviour to the full-linear solution in the high-frequency regime.

For non-uniform shelf/cavity geometries (varying shelf thickness and/or seabed), equations (4) are solved using a step approximation, similar to [35, 32], in which the interval of varying geometry, $0 < x < L$, is divided (uniformly) into N subintervals $x_{n-1} < x < x_n$ for $n = 1, \dots, N$. In each subinterval the geometry is approximated as uniform, with values set to coincide with the varying geometry at the subinterval midpoints $\check{x}_n = (x_{n-1} + x_n) / 2$ $(n = 1, \dots, N)$. The solutions in the nth subinterval, say $\varphi(x) \approx \varphi^{(n)}(x)$ and $\zeta(x) \approx \zeta^{(n)}(x)$ $(x_{n-1} < x < x_n)$, have the form

$$\varphi^{(n)}(x) = \varphi_+^{(n)}(\hat{x}_{n-1}) + \varphi_-^{(n)}(\hat{x}_n) \quad \text{and} \quad \zeta^{(n)}(x) = \zeta_+^{(n)}(\hat{x}_{n-1}) + \zeta_-^{(n)}(\hat{x}_n), \tag{12}$$

where $\hat{x}_n = x - x_n$, and $\varphi_\pm^{(n)}$ and $\zeta_\pm^{(n)}$ are as in (11), with a, H, Γ, and hence μ_m $(m = 1, 2)$, evaluated at $\check{x}_n$. Jump conditions are imposed at the subinterval interfaces $x = x_1, x_2, \dots, x_{N-1}$ to connect potentials $\varphi^{(n)}$ $(n = 1, \dots, N)$, along with continuities of ice shelf displacement, slope, bending moment and shear stress. The amplitudes in each subinterval, and the (approximate) reflection coefficient are found using the recursive algorithm of [3].

Fig. 2(b) shows the time taken to compute the reflection coefficient to three decimal place accuracy (on a standard desktop computer) versus shelf length, L. The shelf thickness increases linearly from the shelf front to the grounding line, and the seabed beneath the shelf shoals linearly towards land (as in Fig. 1), as defined by

$$D(x) = D_0 \left(\frac{1}{s} + \frac{(s^2 - 1)\,x}{s\,L} \right) \quad \text{and} \quad h(x) = h_0 \left(1 - \frac{(s - 1)\,x}{s\,L} \right), \tag{13}$$

for mean thickness $D_0 = 200\,\mathrm{m}$, $h_0 = 500\,\mathrm{m}$, and slope parameter $s = 1.5$. The number of subintervals required increases as the shelf length increases, with $N = 11$ for $L = 1\,\mathrm{km}$ and $N = 252$ for $L = 500\,\mathrm{km}$. Consequently, the time taken increases with increasing shelf length. But, the time taken is $< 1.5\,\mathrm{s}$, even for the longest shelf considered, $L = 500\,\mathrm{km}$.
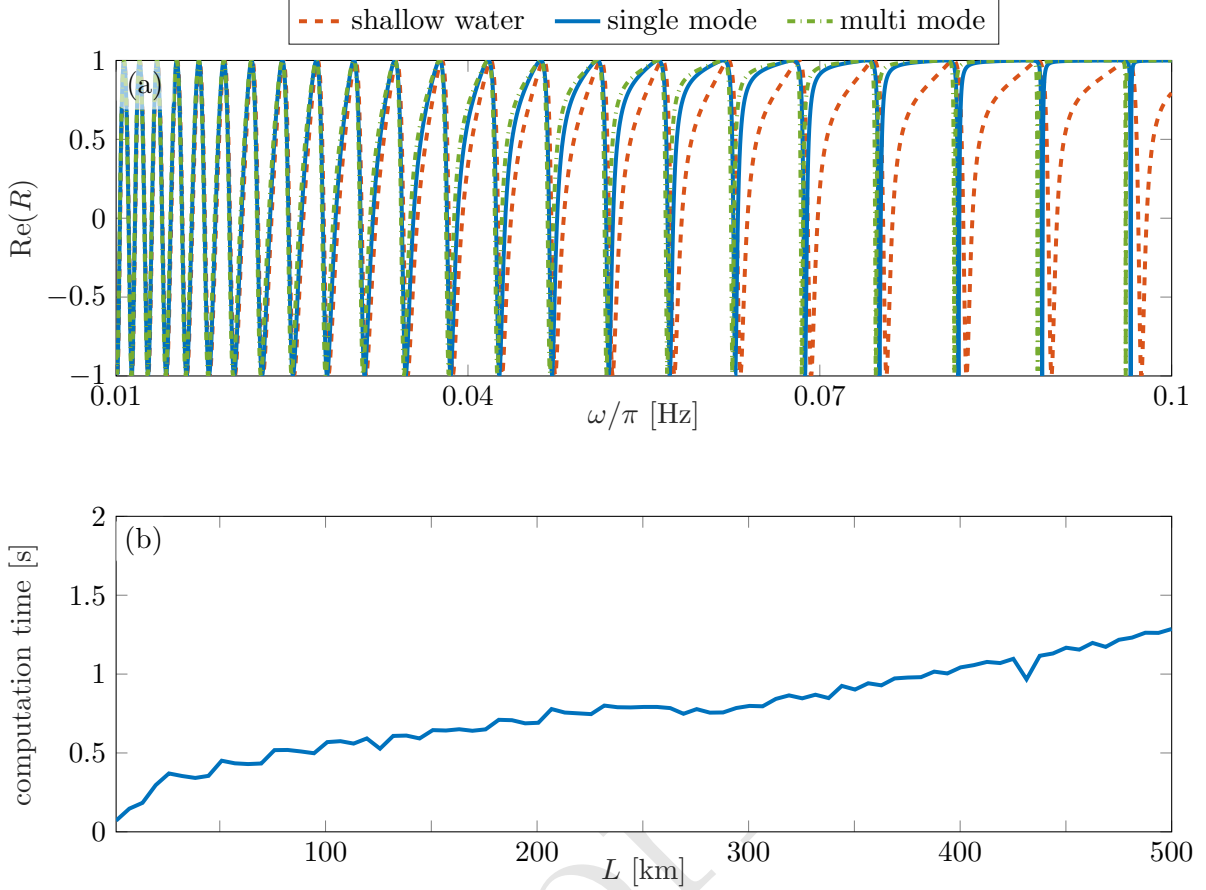
5

Figure 2: (a) Comparison of the real part of reflection coefficient versus frequency, given by the shallow-water approximation, single-mode approximation and multi-mode approximation (ten modes). (b) Computation time to find the reflection coefficient to three decimal places, versus shelf length, for linearly thickening shelf and shoaling seabed (13).

3   Uniform shelf/cavity geometry

Fig. 3(a) shows the normalised maximum shelf displacement, $\tilde{\zeta}_{\mathrm{max}}$, versus frequency for $D = 200\,\mathrm{m}$ and $h = h_0 = 300\,\mathrm{m}$, where

$$\tilde{\zeta}_{\mathrm{max}} = \frac{1}{A_+} \max_{x \in [0,L]} |\zeta|. \tag{14}$$

Corresponding eigenfrequencies for uncoupled shelf/cavity systems are superimposed. The eigenfrequencies are denoted $\omega_n^{(\mathrm{f})}$ and $\omega_n^{(\mathrm{p})}$ $(n = 1, 2, \ldots)$ for the no-flux, $\varphi'(0) = 0$, and no-pressure, $\varphi(0) = 0$, problems, respectively, where the subscript n indicates the number of nodes of the corresponding eigenfunction. The eigenfrequencies of the uncoupled systems interleave one another, such that $0 < \omega_1^{(\mathrm{f})} < \omega_1^{(\mathrm{p})} < \omega_2^{(\mathrm{f})} < \omega_2^{(\mathrm{p})} < \ldots$.

The maximum displacement experiences a sequence of near-resonant peaks, which become broader and more separated as frequency increases. Each peak is bounded below by an eigenfrequency of the no-flux problem and above by an eigenfrequency of the no-pressure problem. For the lowest frequencies in the considered range, the peaks are approximately equidistant from the bounding no-flux/no-pressure eigenfrequencies. As frequency increases, the peaks tend towards the no-pressure eigenfrequencies, and for the highest considered frequencies the peaks occur very close to the no-pressure eigenfrequencies.
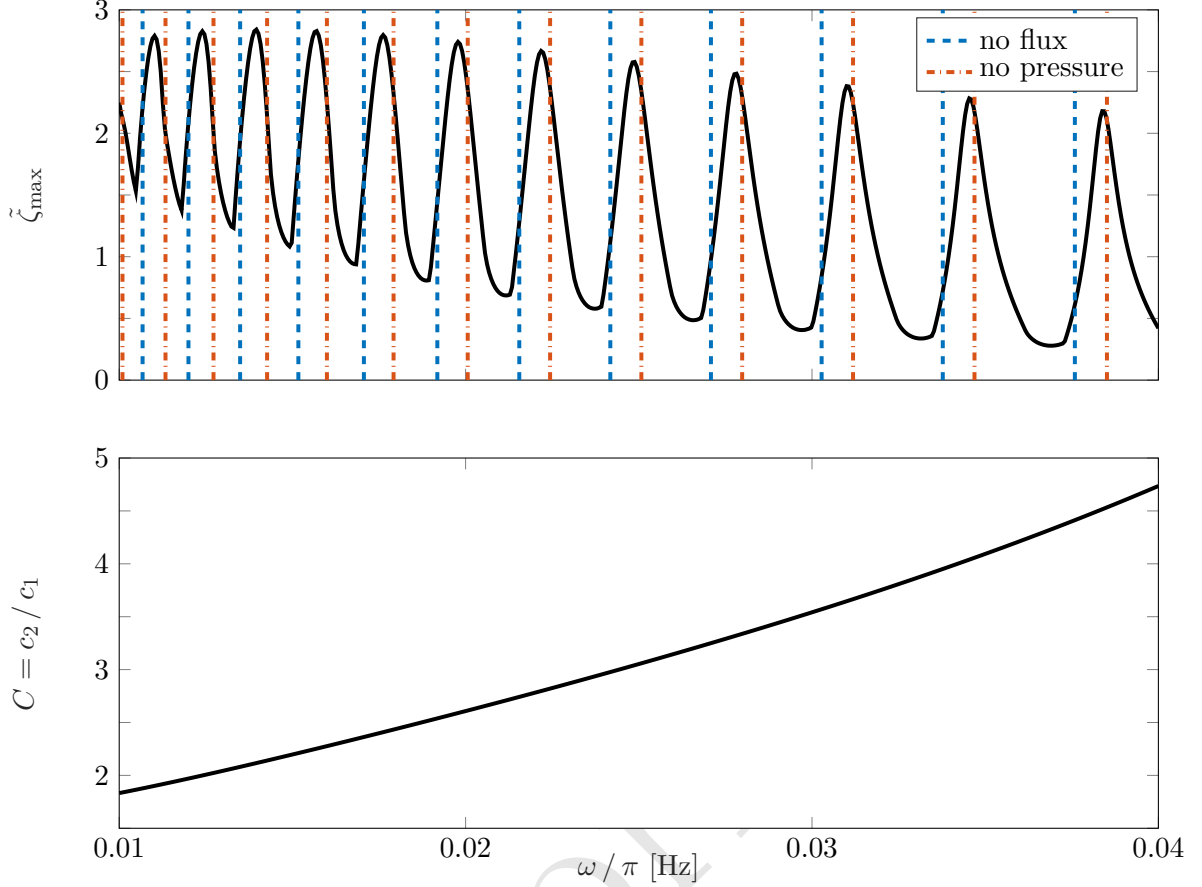
6

Figure 3: (a) Maximum ice shelf displacement versus frequency (black curve), with eigenfrequencies of uncoupled problems superimposed (chained, vertical lines). (b) Coefficient of resonance condition (17) that dictates similarity to no-flux condition ($C \ll 1$) or no-pressure condition ($C \gg 1$), versus frequency.

For a uniform shelf/cavity geometry, jump conditions (8) reduce to

$$v\,\varphi(0) = v_0\,A_+\,(1+R) \quad \text{and} \quad \frac{a}{v}\,\varphi'(0) = \frac{\mathrm{i}\,k\,a_0}{v_0}A_+\,(1-R)\,. \tag{15}$$

Therefore, the no-pressure condition is satisfied when $R = -1$, and the no-flux condition when $R = 1$. Alternatively, jump conditions (15) can be expressed as

$$c_1\left(\frac{\varphi'(0)}{\kappa}\right) + \mathrm{i}\,c_2\,\varphi(0) = 2\,\mathrm{i}\,k\,A_+ \quad \text{and} \quad c_1\left(\frac{\varphi'(0)}{\kappa}\right) - \mathrm{i}\,c_2\,\varphi(0) = -2\,\mathrm{i}\,k\,A_-\,, \tag{16}$$

where $c_1 = \kappa\,a\,v_0\,/\,(a_0\,v)$ and $c_2 = k\,v\,/\,v_0$. The first component of (16) is a boundary condition for the shelf/cavity system, which generalises the no-flux/no-pressure boundary conditions by (i) containing both $\varphi(0)$ and $\varphi'(0)$, and (ii) containing a forcing term (on its right-hand side). The second component of (16) is an expression for the reflected amplitude A_-, which can be applied once φ has been calculated. Resonances occur at frequencies for which non-trivial solutions exist without forcing ($A_+ = 0$), i.e. solutions that satisfy the boundary condition

$$\frac{\varphi'(0)}{\kappa} + \mathrm{i}\,C\,\varphi(0) = 0 \quad \text{where} \quad C \equiv \frac{c_2}{c_1} = \left(\frac{k\,\sinh(\kappa\,H)}{\kappa\,\sinh(k_0\,H)}\right)^2 \frac{2\,k\,h_0 + \sinh(2\,k\,h_0)}{2\,\kappa\,H + \sinh(2\,\kappa\,H)}. \tag{17}$$

7

Resonance condition (17) approximates the no-flux condition if $C \ll 1$ and the no-pressure condition if $C \gg 1$. Fig. 3(b) shows the coefficient C versus ω/π for the problem considered in panel (a). The coefficient monotonically increases with increasing frequency, with minimum value $C \approx 1.83$ for $\omega/\pi = 0.01\,\mathrm{Hz}$ and maximum value $C \approx 4.72$ for $\omega/\pi = 0.04\,\mathrm{Hz}$, which explains why the peak displacements tend towards the no-pressure eigenfrequencies as frequency increases. It can be shown that $C \to \sqrt{h_0/H} \approx 1.58$ as $\omega \to 0$, so that the peaks will not tend towards the no-flux eigenfrequencies for frequencies below the interval of interest.
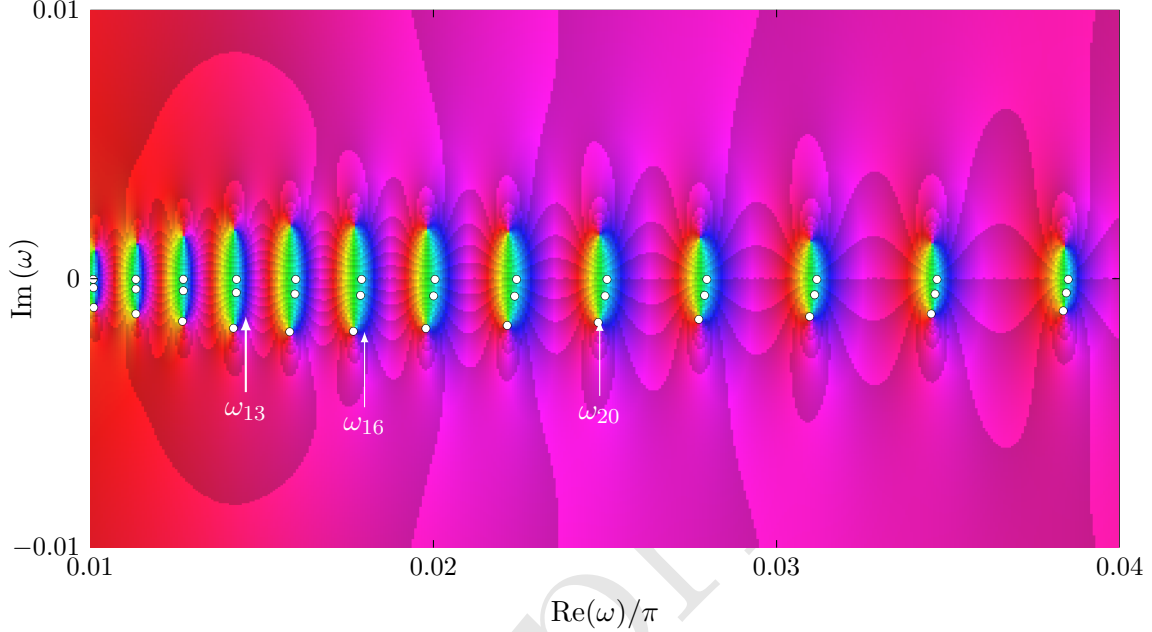

Figure 4: Visualisation of the complex-valued reflection coefficient, R, in complex-frequency space, overlaid with steps of the homotopy method to find the complex-resonant frequencies, ω_n, using two steps ($\hbar = 0.5$), and starting at the no-pressure eigenfrequencies on the real-frequency axis.

Complex resonances satisfy the resonance condition (17). They occur at complex-valued frequencies $\omega = \omega_m$ ($m = 1, 2\ldots$), in the lower-half complex plane, which have small imaginary parts and real parts close to the near-resonant frequencies. The ordering is consistent with the eigenfrequencies of the uncoupled problems (as described below), and typically such that $0 < \mathrm{Re}(\omega_1) < \mathrm{Re}(\omega_2) < \ldots$.

It can be deduced from (16) that $|R| \to \infty$ as $\omega \to \omega_m$ ($m = 1, 2\ldots$), i.e. the reflection coefficient has poles at the complex-resonant frequencies. For a complex-valued ω, the reflection coefficient satisfies the property

$$R(\overline{\omega}) = |R(\omega)|^{-1}\, \mathrm{e}^{\mathrm{i}\arg\{R(\omega)\}}. \tag{18}$$

Therefore, the poles of the reflection coefficient at the complex-resonant frequencies in the lower-half complex plane are associated with zeros in the upper-half complex plane, $R(\overline{\omega}_m) = 0$ ($m = 1, 2\ldots$).

Fig. 4 is a visualisation of the complex-valued reflection coefficient as a function of complex frequency, for the problem considered in Fig. 3, in which the colour represents the phase and the hue the magnitude [36, 24]. The series of predominantly green oval shapes are frequency regions around the near resonances (Fig. 3a). Zeros of the reflection coefficient occur close to the upper tips of the ovals, and poles close to the lower tips (indicated by the lower row of white bullets, as described below).

An efficient algorithm is generated to calculate the complex-resonant frequencies, in which the real-valued eigenfrequencies for the uncoupled problems are used as initial guesses. The algorithm is based on a homotopy between the uncoupled and coupled problems in terms of scattering matrices and

vectors. For the coupled problem, the shelf-front conditions are expressed by the scattering relations

$$A_- = \mathcal{R}_- A_+ + \mathcal{T}_+ \mathbf{B}_- \quad \text{and} \quad \mathbf{B}_+ = \mathcal{T}_- A_+ + \mathcal{R}_+ \mathbf{B}_-, \tag{19}$$

where $\mathbf{B}_\pm = [B_{0\pm}, B_{1\pm}, B_{2\pm}]^T$. In (19), $\mathcal{R}_-(\omega)$ is a 1×1 reflection matrix, $\mathcal{R}_+(\omega)$ is a 3×3 reflection matrix, and $\mathcal{T}_-(\omega)$ and $\mathcal{T}_+(\omega)$ are length 3 column and row transmission vectors, respectively. The shelf-front conditions for the uncoupled problems are expressed as

$$\mathbf{B}_+ = \mathcal{R}_\text{f} \mathbf{B}_- \quad \text{and} \quad \mathbf{B}_+ = \mathcal{R}_\text{p} \mathbf{B}_- \tag{20}$$

for the no-flux and no-pressure problem, respectively, where $\mathcal{R}_\text{f/p}$ are 3×3 reflection matrices. Treating the uncoupled problems as coupled problems with the restrictions $A_- = -A_+$ for the no-pressure problem ($R = -1$) and $A_- = A_+$ for the no-flux problem ($R = 1$), derives the expressions

$$\mathcal{R}_\text{f} = \mathcal{R}_+ + \mathcal{T}_- \left(1 - \mathcal{R}_-\right)^{-1} \mathcal{T}_+ \quad \text{and} \quad \mathcal{R}_\text{p} = \mathcal{R}_+ - \mathcal{T}_- \left(1 + \mathcal{R}_-\right)^{-1} \mathcal{T}_+, \tag{21}$$

which relate the reflection matrices for the uncoupled problems to the reflection matrices and transmission vectors for the coupled problem.

The eigenfrequencies of the uncoupled problems are found by searching along the (positive) real axis of frequency space for frequencies such that $\det(\mathcal{M}_\text{f}) = 0$ for the no-flux condition and $\det(\mathcal{M}_\text{p}) = 0$ for the no-pressure condition, where $\mathcal{M}_\text{f/p}(\omega)$ are the 6×6 matrices

$$\mathcal{M}_\text{f/p}(\omega) = \begin{pmatrix} \mathcal{I} & -\mathcal{R}_\text{f/p}(\omega) \, \mathcal{E}(\omega) \\ -\mathcal{R}_\text{ld}(\omega) \, \mathcal{E}(\omega) & \mathcal{I} \end{pmatrix}. \tag{22}$$

The corresponding eigenvectors are $\mathbf{v}_n^{(\text{f/p})}$ ($n = 1, 2, \ldots$), such that

$$\mathcal{M}_\text{f/p}(\omega_n^{(\text{f/p})}) \, \mathbf{v}_n^{(\text{f/p})} = \mathbf{0}. \tag{23}$$

In (22), $\mathcal{I}$ is the 3×3 identity matrix, $\mathcal{E} = \text{diag}\{e^{i \kappa L}, e^{i \mu_1 L}, e^{i \mu_2 L}\}$, and $\mathcal{R}_\text{ld}$ is a 3×3 grounding-line reflection matrix defined by the relation $\mathbf{B}_- = \mathcal{R}_\text{ld} \mathbf{B}_+$, where the amplitudes $B_{m\pm}$ ($m = 0, 1, 2$) are associated to the functions

$$\varphi(x) = \varphi_+(x - L) + \varphi_-(x - L) \quad \text{and} \quad \zeta(x) = \zeta_+(x - L) + \zeta_-(x - L), \tag{24}$$

which satisfy the grounding-line boundary conditions, i.e. the second and third components of (6).

Complex resonances occur when $\det(\mathcal{M}) = 0$, for the 6×6 matrix

$$\mathcal{M}(\omega) = \begin{pmatrix} \mathcal{I} & -\mathcal{R}_+(\omega) \, \mathcal{E}(\omega) \\ -\mathcal{R}_\text{ld}(\omega) \, \mathcal{E}(\omega) & \mathcal{I} \end{pmatrix}, \tag{25}$$

i.e. when the second component of (19) is satisfied for $A_+ = 0$, along with the grounding-line conditions. The corresponding eigenvectors are $\mathbf{v}_n$ ($n = 1, 2, \ldots$), such that $\mathcal{M}(\omega_n) \, \mathbf{v}_n = \mathbf{0}$. Matrix $\mathcal{M}$ is almost identical to matrices $\mathcal{M}_\text{f/p}$ defined in (22), with the only difference that the reflection matrix $\mathcal{R}_+$ replaces $\mathcal{R}_\text{f/p}$.

Therefore, a homotopy is created by defining the matrix

$$\mathcal{M}_\hbar(\omega) = \begin{pmatrix} \mathcal{I} & -\mathcal{R}_\hbar(\omega) \, \mathcal{E}(\omega) \\ -\mathcal{R}_\text{ld}(\omega) \, \mathcal{E}(\omega) & \mathcal{I} \end{pmatrix}, \tag{26}$$

for homotopy parameter $\hbar \in [0, 1]$, and corresponding eigenfrequencies $\omega_{\hbar,n}$ and eigenvectors $\mathbf{v}_{\hbar,n}$ ($n = 1, 2 \ldots$), where, either

$$\mathcal{R}_\hbar = \mathcal{R}_+ + (1 - \hbar) \, \mathcal{T}_- \left(1 - \mathcal{R}_-\right)^{-1} \mathcal{T}_+ \tag{27a}$$

9

for the no-flux problem, or

$$\mathcal{R}_\hbar = \mathcal{R}_+ - (1 - \hbar)\,\mathcal{T}_-\,(1 + \mathcal{R}_-)^{-1}\,\mathcal{T}_+ \tag{27b}$$

for the no-pressure problem. At $\hbar = 0$, $\mathcal{R}_0 = \mathcal{R}_{\mathrm{f}}$ for (27a) and $\mathcal{R}_0 = \mathcal{R}_{\mathrm{p}}$ for (27b), and $\mathcal{R}_1 = \mathcal{R}_+$ at $\hbar = 1$ in either case.

The complex-resonant frequencies and corresponding eigenvectors are found in discrete steps of the homotopy parameter, say $\hbar_0 = 0 < \hbar_1 < \ldots < \hbar_J = 1$, starting at either the no-flux problem

$$\omega_{\hbar_0,n} = \omega_n^{(\mathrm{f})} \quad \text{and} \quad \mathbf{v}_{\hbar_0,n} = \mathbf{v}_n^{(\mathrm{f})} \tag{28a}$$

or the no-pressure problem

$$\omega_{\hbar_0,n} = \omega_n^{(\mathrm{p})} \quad \text{and} \quad \mathbf{v}_{\hbar_0,n} = \mathbf{v}_n^{(\mathrm{p})}. \tag{28b}$$

At each homotopy step, an iterative algorithm is used (adapted from [29]), in which

$$\omega_{\hbar_j,n} = \lim_{q \to \infty} \omega_{\hbar_j,n}^{(q)} \quad \text{and} \quad \mathbf{v}_{\hbar_j,n} = \lim_{q \to \infty} \mathbf{v}_{\hbar_j,n}^{(q)}, \tag{29}$$

using the update formula

$$\omega_{\hbar_j,n}^{(q+1)} = \omega_{\hbar_j,n}^{(q)} + \Delta_{\hbar_j}\left(\omega_{\hbar_j,n}^{(q)}, \mathbf{v}_{\hbar_j,n}^{(q)}\right) \tag{30a}$$

$$\text{and} \quad \mathbf{v}_{\hbar_j,n}^{(q+1)} = \Delta_{\hbar_j}\left(\omega_{\hbar_j,n}^{(q)}, \mathbf{v}_{\hbar_j,n}^{(q)}\right)\,\mathbf{q}_\hbar\left(\omega_{\hbar_j,n}^{(q)}, \mathbf{v}_{\hbar_j,n}^{(q)}\right) \tag{30b}$$

for $q = 0, 1, \ldots$, where

$$\Delta_\hbar(\omega, \mathbf{v}) = \frac{-\mathbf{q}_\hbar^T\,\mathcal{M}_\hbar(\omega)\,\mathbf{q}_\hbar}{\mathbf{q}_\hbar^T\,\mathcal{M}_\hbar'(\omega)\,\mathbf{q}_\hbar} \quad \text{and} \quad \mathbf{q}_\hbar(\omega, \mathbf{v}) = -\mathrm{inv}\{\mathcal{M}_\hbar(\omega)\}\,\mathcal{M}_\hbar'(\omega)\,\mathbf{v}. \tag{31}$$

The iterative algorithm is initialised with $\omega_{\hbar_j,n}^{(0)} = \omega_{\hbar_{j-1},n}$ and $\mathbf{v}_{\hbar_j,n}^{(0)} = \mathbf{v}_{\hbar_{j-1},n}$, consistent with the homotopy.

The white bullets on Fig. 4 denote $\omega_{\hbar_j,n}$ for two homotopy steps ($J = 2$), starting from the no-pressure eigenvalues. No more than two homotopy steps are required for other uniform shelf/cavity problems tested (not shown), and often only a single step is sufficient, although the extra step helps ensure the complex resonances are found in certain cases.

Fig. 5 shows the modulus of the complex-resonant eigenfunctions, $\eta_n(x)$, associated with the three complex frequencies labelled in Fig. 4 ($n = 13$, 16, 20), which are defined by the eigenvectors $\mathbf{v}_n$. Corresponding eigenfunctions for the uncoupled problems, $\eta_n^{(\mathrm{f/p})}(x)$, are also shown. All eigenfunctions are normalised so that they have unit magnitude at the shelf front ($x = 0$). Except in the vicinity of the shelf front (where the maximum values of the eigenfunctions occur), the qualitative behaviour of the complex-resonant eigenfunctions is similar to the corresponding no-pressure eigenfunctions. Their peaks occur at similar locations, although the peaks of the complex-resonant eigenfunctions decrease in magnitude with distance along the shelf, in contrast to the peaks for the no-pressure eigenfunctions, which are uniform along the shelf length (similarly for the no-flux eigenfunctions). The local minima of corresponding complex-resonant and no-pressure eigenfunctions occur at approximately the same locations. The no-pressure minima are zeros (nodal points), whereas the complex-resonant minima are smooth troughs. For the highest frequency ($n = 20$), the complex-resonant eigenfunction is similar to the no-pressure eigenfunction along the full shelf length, as can be anticipated from (17) and Fig. 3.

Fig. 6 shows the (a) real and (b) imaginary parts of the reflection coefficient versus real frequency, for the uniform shelf/cavity geometry considered in Figs. 3–4. The Blaschke product $R_{\mathrm{bl}}(\omega)$ is overlaid, where

$$R_{\mathrm{bl}}(\omega) = \prod_{n=1}^\infty r(\omega : \omega_n)\,r(\omega : -\overline{\omega_n}), \quad r(\omega : \varpi) = \frac{\omega - \overline{\varpi}}{\omega - \varpi}. \tag{32}$$
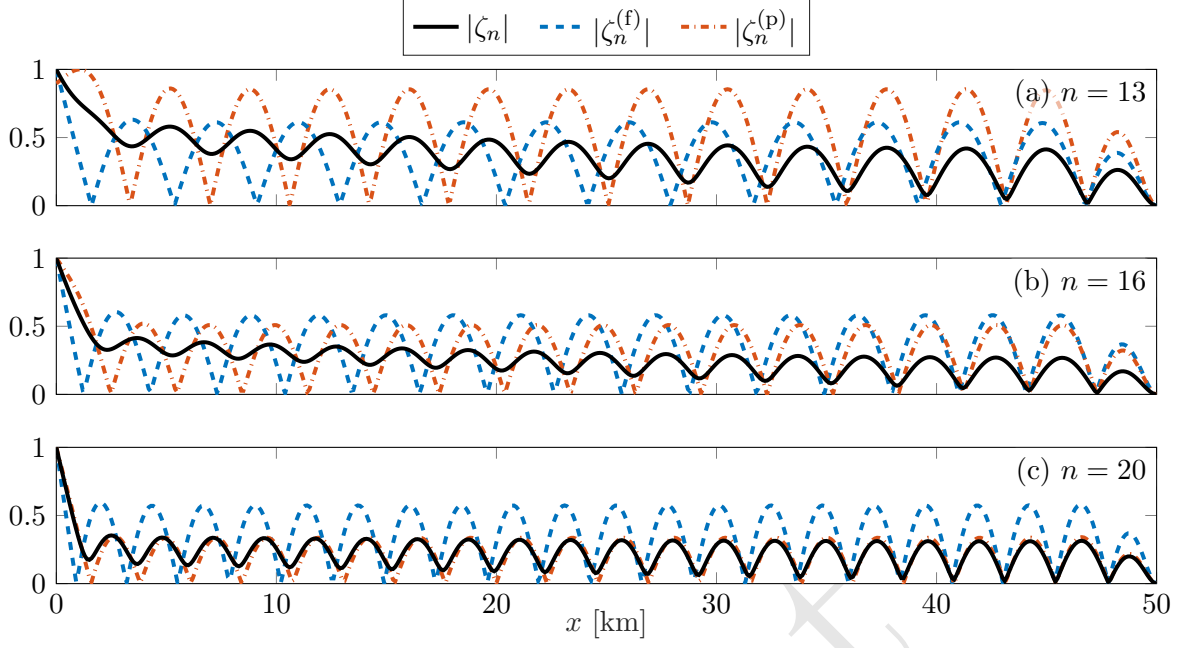
10

Figure 5: Modulus of complex-resonant eigenfunctions, $|\zeta_n|$, and corresponding eigenfunctions of uncoupled problems, $|\zeta_n^{(\mathrm{f})}|$ (no flux) and $|\zeta_n^{(\mathrm{p})}|$ (no pressure).
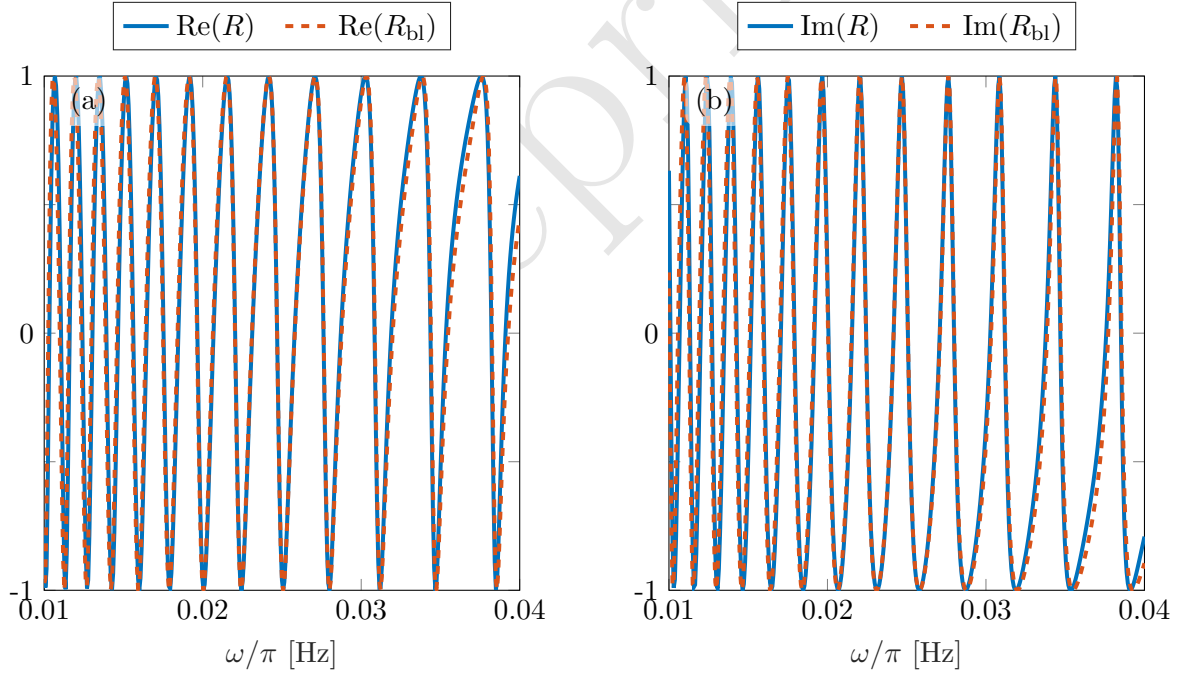

Figure 6: (a) Real and (b) imaginary parts of the reflection coefficient, R, and Blaschke product, R_{bl}, versus frequency.

It closely approximates the reflection coefficient over the frequency range of interest. Each factor $r(\omega : \omega_n)$ in the Blaschke product satisfies

$$r(\mathrm{Re}\{\omega_n\} : \omega_n) = -1 \quad \text{and} \quad r(\omega : \omega_n) \to 1 \quad \text{as} \quad |\omega - \omega_n| \to \infty, \tag{33}$$

confirming association of the complex-resonant frequencies with the eigenvalues of the no-pressure

11

problem (for which $R = -1$). The frequencies at which $R_{\mathrm{bl}} = -1$ are perturbed from $\omega = \mathrm{Re}\{\omega_n\}$ ($n = 1, 2, \ldots$) by the other factors in the product. Consecutive factor pairs satisfy $r(\omega : \omega_n)\,r(\omega : \omega_{n+1}) = 1$ for some $\omega \in (\mathrm{Re}\{\omega_n\}, \mathrm{Re}\{\omega_{n+1}\})$, which approximates eigenfrequencies of the no-flux problem (for which $R = 1$).

For the shallow-water approximation, the equivalent Blaschke product is exact ($R = R_{\mathrm{bl}}$), as the reflection coefficient is a meromorphic function of complex frequency, in addition to $|R| = 1$ for $\omega \in \mathbb{R}$. In contrast, the reflection coefficient given by the single-mode approximation contains branch cuts due to the hyperbolic tangent in dispersion relations (3). The branch cuts cause the Blaschke product to deviate from the reflection coefficient at high frequencies (not shown).
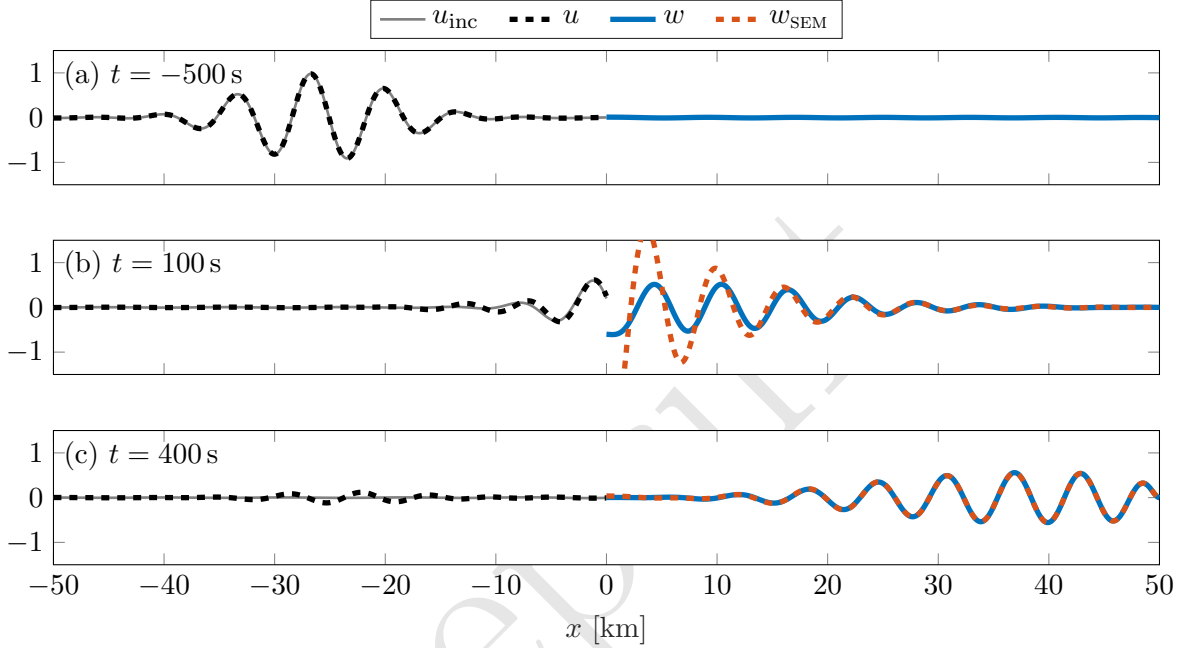

Figure 7: Snapshots of a simulation in which a Gaussian incident wave packet forces shelf vibrations. In the open ocean ($x < 0$), both the incident surface elevation and the full surface elevation (incident plus reflected) are shown. In the shelf/cavity region ($0 < x < L$), the SEM is overlaid for the two largest times shown.

Consider a transient problem, in which ice-shelf vibrations are forced by a unit-amplitude incident wave packet, defined by the Fourier transform in k at $t = 0$

$$\mathcal{F}\{u_{\mathrm{inc}}(x, 0)\} \equiv \hat{f}(k) = \sqrt{\frac{\beta}{\pi}}\, \mathrm{e}^{-\beta\,(k-k_0)^2 - \mathrm{i}\,k\,x_0}, \tag{34}$$

where k_0 is the central wavenumber, β defines the packet width, and x_0 is the physical location of the packet centre at $t = 0$. The shelf displacement is

$$w(x, t) = \mathrm{Re}\left\{\frac{1}{\pi} \int_0^\infty \hat{f}(k)\, \zeta(x)\, \mathrm{e}^{-\mathrm{i}\,\omega\,t}\, \mathrm{d}k\right\}, \tag{35}$$

and a similar expression is used for the open-ocean surface elevation, $u(x, t)$ ($x < 0$).

Fig. 7 shows snapshots of a simulation for the piece-wise uniform geometry considered previously in §3 ($D = 200\,\mathrm{m}$ and $h = h_0 = 300\,\mathrm{m}$), and an incident packet with central wavenumber $k_0 = 0.0009\,\mathrm{m}^{-1}$, $\beta = 2 \times 10^7\,\mathrm{m}^2$ and $x_0 = 0$. Panel (a) shows the instant $t = -500\,\mathrm{s}$, at which the incident packet is travelling towards the shelf, but has not yet reached it. Panel (b) shows the instant $t = 100\,\mathrm{s}$, at which the packet has reached the shelf and forced shelf vibrations. Panel (c) shows an instant $300\,\mathrm{s}$

later, when the vibrations have travelled along the shelf, and the elevation of the ocean surface consists only of reflected waves.

For long times, the shelf vibrations can be approximated by the singularity expansion method (SEM), $w(x,t) \approx w_{\text{SEM}}(x,t)$ $(t \gg 1)$, where

$$w_{\text{SEM}}(x,t) = \sum_{n=1}^{\infty} \text{Re}\{w_n(x,t)\}, \quad \text{in which} \quad w_n = A_n\,\zeta_n(x)\,\mathrm{e}^{-\mathrm{i}\,\omega_n\,t} \quad (n = 1, 2, \dots) \tag{36}$$

are complex modes. The amplitudes A_n are [28]

$$A_n = 2\,\pi\,\mathrm{i}\,\hat{f}(k(\omega_n))\,\frac{\mathbf{u}_n^T\,\mathbf{b}_n}{\mathbf{u}_n^T\,\mathcal{M}'(\omega_n)\,\mathbf{v}_n} \quad \text{where} \quad \overline{\mathcal{M}}^T(\omega_n)\,\mathbf{u}_n = \mathbf{0}, \tag{37}$$

$$\mathbf{b}_n = \left[\left(\mathcal{T}_-(\omega_n)\right)^T, 0, 0, 0\right]^T, \tag{38}$$

and $\hat{f}$ is the analytic extension of (34). The SEM is overlaid on Fig. 7 for the two later times, $t = 100\,\text{s}$ and $400\,\text{s}$. At $t = 100\,\text{s}$ the SEM does not give an accurate approximation of the shelf vibrations. By $t = 400\,\text{s}$ the SEM is indistinguishable from the full solution. The central frequency of the incident packet, $\omega_0 = \omega(k_0)$, is chosen to coincide with the real part of the complex-resonant frequency ω_{16}, so that complex mode w_{16} is strongly excited. The width of the Gaussian causes neighbouring complex modes to be excited, and at $t = 400\,\text{s}$ modes w_{15} and w_{17} are of comparable magnitude to w_{16}, allowing the SEM to capture the travelling wave accurately.
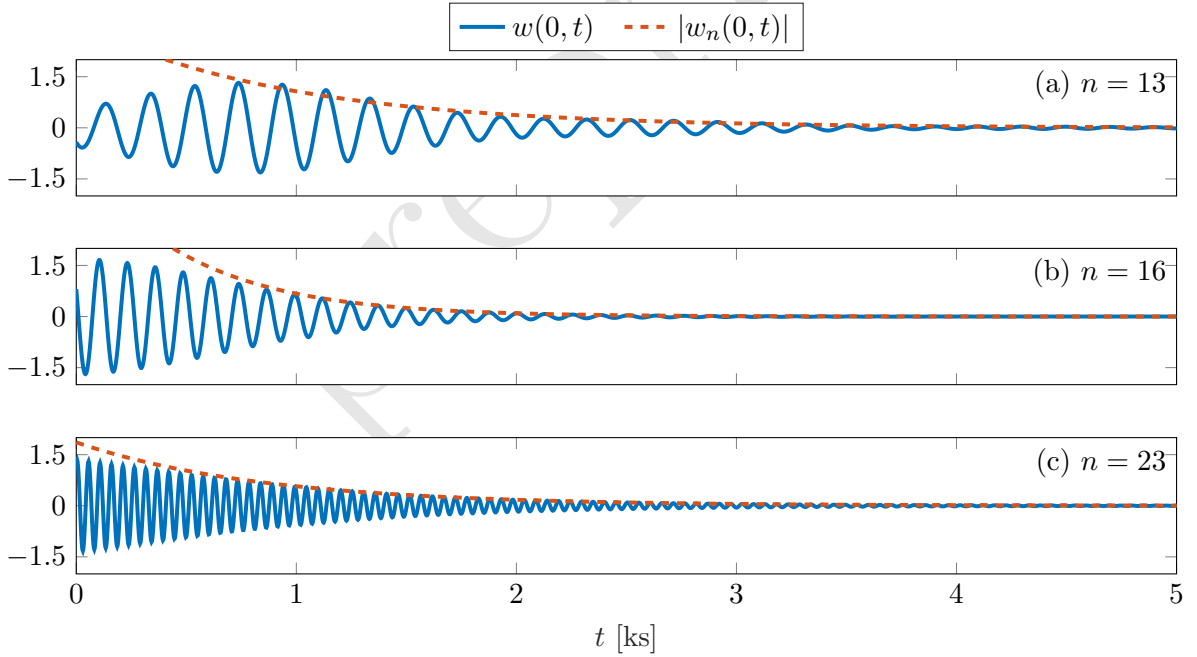

Figure 8: Time series of shelf-front vibration, for incident wave packets where complex mode w_n dominates the SEM at large times. The modulus of the dominant complex mode at the shelf front is overlaid on each time series.

The SEM captures the so-called resonant lifetimes of ice shelf vibrations, i.e. the decay rate in vibrational response to an incident wave packet. If the incident packet is such that one complex-resonant mode dominates for large times, i.e. $w(x,t) \approx w_n(x,t)$ $(t \gg 1)$ for some n, then

$$|w(x,t)| \approx |w_n(x,t)| = |A_n\,\zeta_n(x)|\,\mathrm{e}^{\text{Im}\{\omega_n\}t} \quad \text{for} \quad t \gg 1. \tag{39}$$

Fig. 8 shows time series of the shelf front responses to Gaussian incident wave packets, with $x_0 = L$. The packets have central frequencies such that $\omega_0 = \mathrm{Re}\{\omega_n\}$ for $n = 13$, 16 and 23, and are sufficiently narrow, $\beta = 5 \times 10^8\,\mathrm{m}^2$, that w_n dominates the SEM. The modulus of $w_n(0, t)$ is overlaid on the time series, and provides an envelope for the full solution at large times, and hence the decay rate, as indicated by (39).

4   Non-uniform geometry

The non-uniform geometries are restricted to shelf thickness variations, as they have a greater influence on resonant responses than equivalent seabed variations [27], and, as will be shown, they change the qualitative behaviours of the complex resonances. Linear shelf thickening of the form given in the first component of (13) is considered, with mean thickness $D_0 = 200\,\mathrm{m}$, slope parameter $s \in [1, 2]$, and over a flat seabed of depth $h = h_0 = 500\,\mathrm{m}$. The increased water depth, in comparison to §3 where $h = h_0 = 300\,\mathrm{m}$, accommodates the shelf draught towards the grounding line for larger values of s.
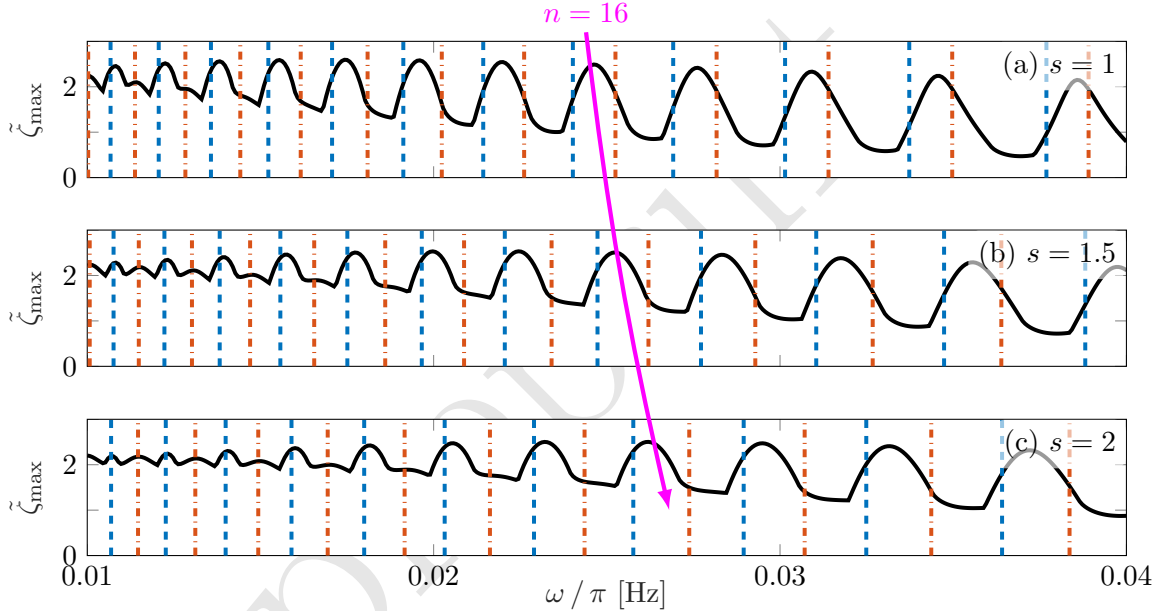

Figure 9: Maximum ice shelf displacement versus frequency, with uncoupled eigenfrequencies overlaid, for shelf of (a) uniform thickness, (b) intermediate slope, and (c) large slope. Frequency upshift of $n = 16$ peak as slope increases is indicated.

Fig. 9 shows the normalised maximum shelf displacement versus frequency, with uncoupled eigenfrequencies superimposed, for a uniform shelf ($s = 1$), intermediate slope ($s = 1.5$) and large slope ($s = 2$). The results for the uniform shelf are broadly similar to the those for the uniform shelf with shallower depth shown in Fig. 3, although the deeper water causes a frequency upshift, so that the peak bounded by the $n = 16$ eigenfrequencies (labelled) is close to the centre of the frequency range, compared to $n = 20$ for the shallower water depth (Fig. 4). At the lower end of the frequency range, small peaks/inflections occur between the prominent near-resonant peaks, and coincide with the no-pressure eigenfrequencies. (The feature also occurs for the shallower water, but at frequencies below the range considered.)

Shelf thickening frequency upshifts the maximum displacement, as indicated by the labelled $n = 16$ peaks. The troughs between the peaks become shallower, due to the ice becoming thinner at the shelf front where the maximum displacements occur. The near-resonant peaks remain bounded above and below by eigenfrequencies of the uncoupled problems, and tend towards the no-pressure

eigenfrequencies as frequency increase. However, frequency upshifting of the peaks, combined with increased separation of the no-flux and no-pressure eigenfrequencies as slope increases, results in the peaks being slightly closer to the no-flux eigenfrequencies than the no-pressure eigenfrequencies over the considered frequency range for the largest slope ($s = 2$).
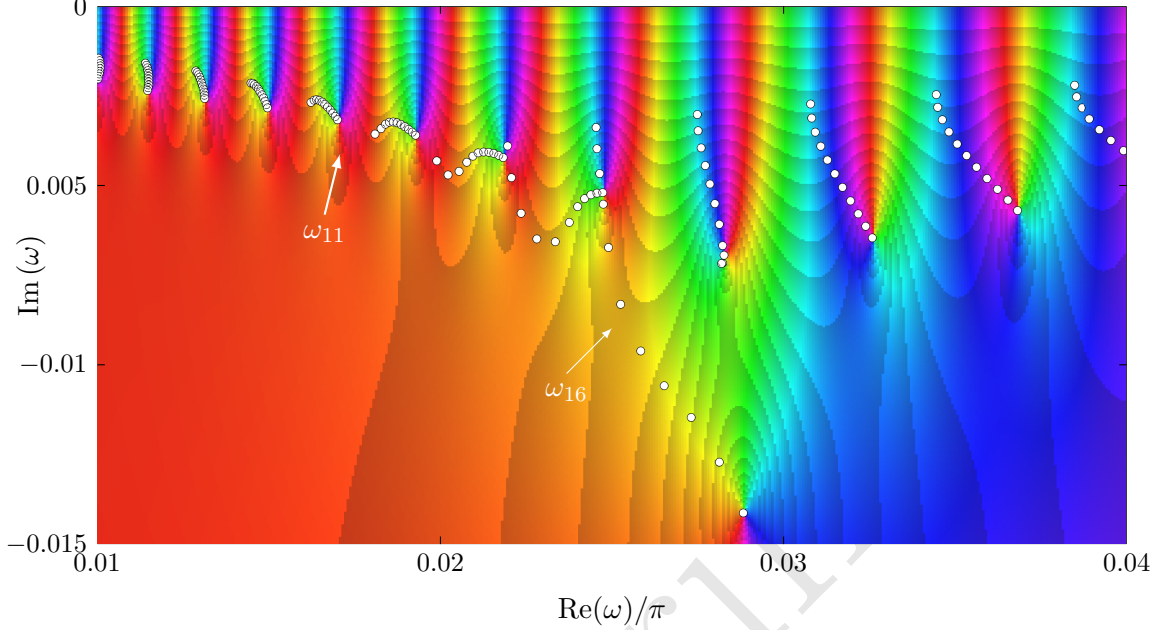

Figure 10: Complex-resonant frequencies for linearly thickening shelves with slope parameter $s = 1$, $1.1, \ldots, 2$, superimposed on a visualisation of the complex-valued reflection coefficient in the lower-half complex frequency plane.

Fig. 10 shows complex-resonant frequencies ω_n in the lower-half complex frequency plane, for thickening shelves with slopes $s = 1, 1.1, \ldots, 2$. The background is the complex-valued reflection coefficient for the largest slope ($s = 2$). Increasing the slope tends to push the ω_n away from the real axis (decreasing imaginary parts), and upshift their real parts. For complex-resonant frequencies with real parts at the lower end of the range of interest, $\mathrm{Re}\{\omega_n\}/\pi < 0.02\,\mathrm{Hz}$, the changes are relatively small. For real parts at the higher end, $\mathrm{Re}\{\omega_n\}/\pi > 0.03\,\mathrm{Hz}$, the changes are large but regular, i.e. monotonically increasing real part and decreasing imaginary part. For mid-range frequencies, $0.02 < \mathrm{Re}\{\omega_n\}/\pi < 0.03\,\mathrm{Hz}$, the changes can be large and irregular. Both ω_{14} and ω_{15} initially move away from the real axis as slope increases, up to $s = 1.1$ and $s = 1.4$, respectively, but then move back towards the real axis, whilst their real parts monotonically increase. The evolution of ω_{16} with increasing shelf slope is regular, but the increases in real part and decreases in imaginary part are far greater than the other frequencies. At the largest slope, $s = 2$, its real part is greater than the real part of ω_{17}, and it is over twice as far from the real axis than the other complex-resonant frequencies.

Fig. 11 shows moduli of complex-resonant eigenfunctions, for the uniform shelf ($s = 1$), intermediate slope ($s = 1.5$) and large slope ($s = 2$). Panel (a) shows a typical low-frequency case ($n = 11$), and panel (b) eigenfunctions corresponding to complex-resonant frequencies that move farthest from the real axis ($n = 16$). For $n = 11$, increasing slope exacerbates the decrease in magnitude of the peaks along the shelf, and reduces the oscillation amplitude. The qualitative properties of the eigenfunctions are almost identical. In contrast, for $n = 16$, increasing the slope damps out eigenfunction oscillations, and at the largest slope ($s = 2$) the eigenfunction is approximately a simple decaying exponential.

The large changes in complex resonance $n = 16$ with increasing shelf slope, relative to the surrounding complex resonances, have a major effect on the excitation of the resonance in transient
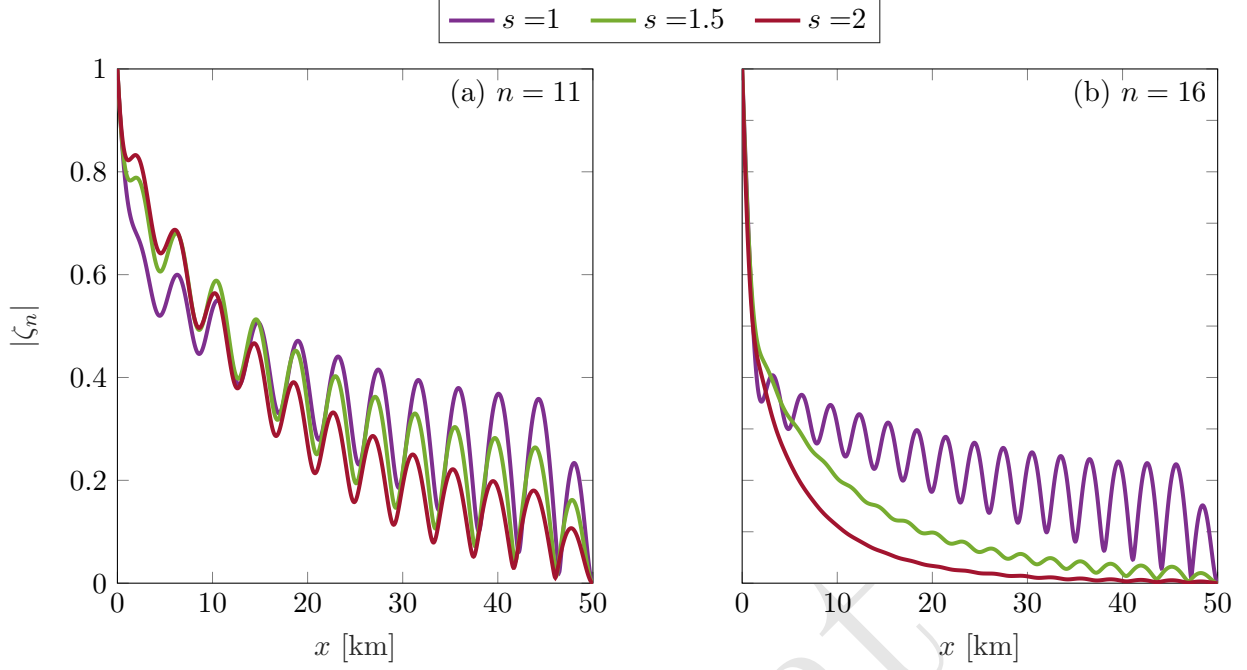
Figure 11: Modulus of complex-resonant eigenfunctions, for shelf of uniform thickness ($s = 1$), inter-mediate slope ($s = 1.5$) and large slope ($s = 2$), and corresponding to the complex-resonant frequencies ω_n labelled in Fig. 10 ($n = 11$ and 16).
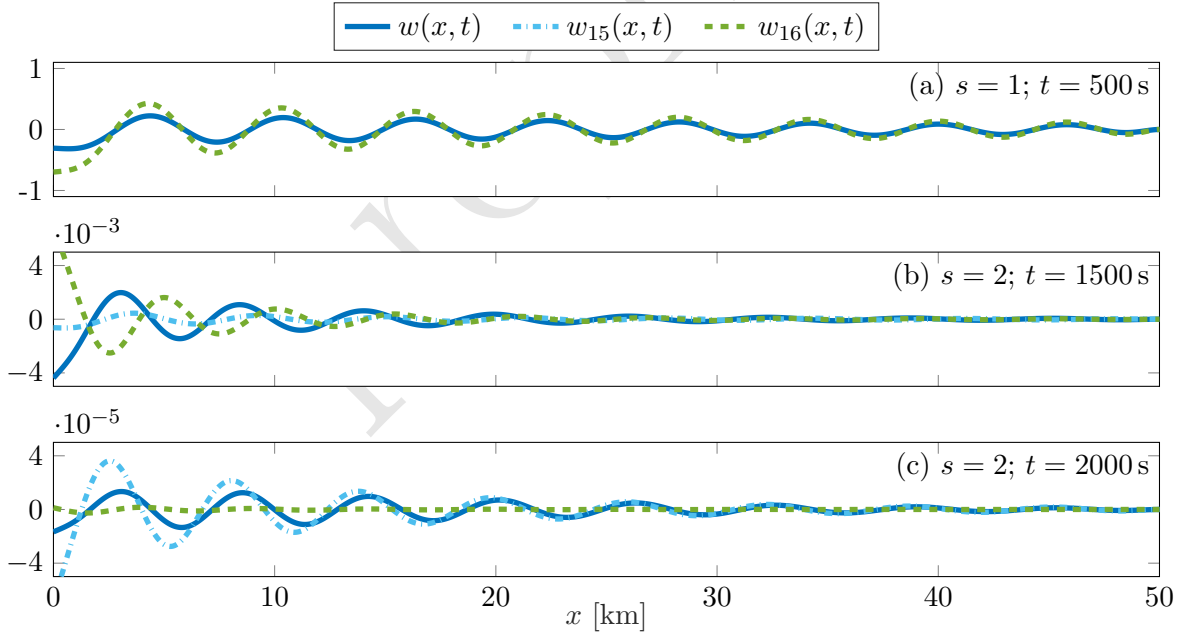

Figure 12: (a) Snapshot of uniform-shelf vibration profile ($s = 1$), forced by incident wave packet with central frequency that coincides with the peak of the maximum shelf displacement corresponding to $n = 16$ (as indicated in Fig. 9a). Corresponding profile of complex mode w_{16} at the same time instant is superimposed. (b–c) Similar snapshots for linearly thickening shelf with large slope ($s = 2$). Profiles of complex mode w_{15} are also included.

problems. Fig. 12 shows snapshots from simulations that exemplify the phenomenon. Panel (a) shows

a shelf vibration profile from a simulation in which the uniform shelf is forced by a Gaussian incident packet (34) with central frequency $\omega_0 / \pi = 0.0247\,\text{Hz}$, width parameter $\beta = 5 \times 10^8\,\text{m}^2$ and $x_0 = L$. The central frequency coincides with the near-resonant maximum-displacement peak bounded by the $n = 16$ eigenfrequencies (labelled in Fig. 9a). Corresponding complex-resonant mode w_{16} is superimposed, and at the instant shown ($t = 500\,\text{s}$), the mode approximates the shelf vibration profile well, and becomes indistinguishable from it at later times (not shown). Therefore, the incident packet centred at the $n = 16$ near resonance excites the associated complex resonance.

Panels (b–c) show snapshots from an analogous simulation, in which the large-slope thickening shelf ($s = 2$) is forced by a Gaussian incident packet, similar to the one used for panel (a). The central frequency of the packet is upshifted to $\omega_0 / \pi = 0.0262\,\text{Hz}$ to coincide with the $n = 16$ near-resonant peak for $s = 2$ (labelled in Fig. 9c). Complex-resonant modes w_{15} and w_{16} are superimposed on both panels. At the instant shown in panel (b) ($t = 1500\,\text{s}$), both modes are of similar magnitude, but neither mode approximates the shelf vibration profile well, despite the snapshot shown being $1000\,\text{s}$ later than in panel (a) and the displacements two orders of magnitude smaller. Panel (c) shows an instant $500\,\text{s}$ later, at which mode w_{16} has decayed to approximately zero, and mode w_{15} approximates the shelf vibration profile reasonably well. Therefore, the incident packet centred at the $n = 16$ near-resonant peak has not excited the associated complex-resonant mode, but, rather, neighbouring mode w_{15}.

5   Conclusions

Ice-shelf vibrations forced by incident waves from the open ocean were modelled using combined linear thin-plate and potential-flow theories. In contrast to previous studies of wave–shelf interactions, a single-mode approximation was used for the vertical structure in the open ocean and sub-shelf water cavity. The single-mode approximation was shown to give accurate solutions over the frequency range of interest, and generate insights into the links between near-resonant shelf vibrations and uncoupled shelf/cavity problems. A step approximation was used to solve problems in which the shelf thickness and seabed beneath the shelf vary over distance. Using the step approximation, frequency-domain problems for shelves hundreds of kilometres in length were calculated in approximately one second.

The near-resonant shelf vibrations were shown to be connected with complex resonances, which exist for frequencies in the lower-half frequency plane. A homotopy was derived between the uncoupled problems and complex resonances, and was used to create an efficient algorithm to calculate the complex resonances. The complex resonances were used in a Blaschke product, which was shown to approximate the reflection coefficient in the frequency regime of interest. Further, the complex resonances were used in the singularity expansion method to capture the large-time responses of the shelf to incident wave packets.

Ice-shelf thickening was shown, in general, to push the complex-resonant frequencies away from the real axis, and increase their real parts. Mid-range frequencies were found to be most affected by shelf thickening. One complex-resonant frequency, in particular, was shown to move much farther from the real axis than the other frequencies. The behaviour was connected with the phenomenon of the near-resonance becoming difficult to excite with an incident wave packet.

Acknowledgments

References

[1] L. G. BENNETTS, N. R. T. BIGGS, AND D. PORTER, *A multi-mode approximation to wave scattering by ice sheets of varying thickness*, J. Fluid Mech., 579 (2007), pp. 413–443.

[2] L. G. BENNETTS, N. R. T. BIGGS, AND D. PORTER, *The interaction of flexural-gravity waves with periodic geometries*, Wave Motion, 46 (2009), pp. 57–73.

[3] L. G. BENNETTS AND V. A. SQUIRE, *Wave scattering by multiple rows of circular ice floes*, J. Fluid Mech., 639 (2009), pp. 213–238.

[4] P. D. BROMIRSKI, A. DIEZ, P. GERSTOFT, R. A. STEPHEN, T. BOLMER, D. A. WIENS, R. ASTER, AND N. NYBLADE, *Ross Ice Shelf vibrations*, Geophys. Res. Lett., 42 (2015), pp. 7589–7597.

[5] K. M. BRUNT, E. A. OKAL, AND D. R. MACAYEAL, *Antarctic ice-shelf calving triggered by the Honshu (Japan) earthquake and tsunami, March 2011*, J. Glaciol., 57 (2011), pp. 785–788.

[6] L. M. CATHLES, E. A. OKAL, AND D. R. MACAYEAL, *Seismic observations of sea swell on the floating Ross Ice Shelf, Antarctica*, J. Geophys. Res., 114 (2009).

[7] P. G. CHAMBERLAIN AND D. PORTER, *Scattering and near-trapping of water waves by axisymmetric topography*, J. Fluid Mech., 388 (1999), pp. 335–354.

[8] Z. CHEN, P. D. BROMIRSKI, P. GERSTOFT, R. A. STEPHEN, W. S. LEE, S. YUN, S. D. OLINGER, R. C. ASTER, D. A. WIENS, AND A. A. NYBLADE, *Ross Ice Shelf icequakes associated with ocean gravity wave activity*, Geophys. Res. Lett., 46 (2019), pp. 8893–8902.

[9] D. V. EVANS AND R. PORTER, *Trapping and near-trapping by arrays of cylinders in waves*, Appl. Ocan Res., 19 (1997), pp. 83–99.

[10] C. HAZARD AND M. LENOIR, *Determination of scattering frequencies for an elastic floating body*, SIAM J. Math. Anal., 24 (1993), pp. 1458–1514.

[11] C. HAZARD AND F. LORET, *The singularity expansion method applied to the transient motions of a floating elastic plate*, Math. Model. Numer. Anal., 41 (2007), pp. 925–943.

[12] G. HOLDSWORTH AND J. E. GLYNN, *Iceberg calving from floating glaciers by a vibrating mechanism*, Nature, 274 (1978), pp. 464–466.

[13] M. ILYAS, M. H. MEYLAN, B. LAMICHHANE, AND L. G. BENNETTS, *Time-domain and modal response of ice shelves to wave forcing using the finite element method*, J. Fluids Struct., 80 (2018), pp. 113–131.

[14] B. KALYANARAMAN, L. G. BENNETTS, B. LAMICHHANE, AND M. H. MEYLAN, *On the shallow-water limit for modelling ocean-wave induced ice-shelf vibrations*, Wave Motion, 90 (2019), pp. 1–16.

[15] B. KALYANARAMAN, M. H. MEYLAN, L. G. BENNETTS, AND B. P. LAMICHHANE, *A coupled fluid-elasticity model for the wave forcing of an ice-shelf*, J. Fluids Struct., 97 (2020), p. 103074.

[16] Y. V. KONOVALOV, *Ice-shelf vibrations modeled by a full 3-D elastic model*, Annals Glaciol., 60 (2019), pp. 68–74.

[17] B. P. LIPOVSKY, *Ice Shelf Rift Propagation and the Mechanics of Wave-Induced Fracture*, J. Geophys. Res., 123 (2018), pp. 4014–4033.

[18] D. R. MacAyeal, E. A. Okal, R. C. Aster, J. N. Bassis, K. M. Brunt, L. M. Cathles, R. Drucker, H. A. Fricker, Y.-J. Kim, S. Martin, M. H. Okal, O. V. Sergienko, M. P. Sponsler, and J. E. Thom, *Transoceanic wave propagation links iceberg calving margins of Antarctica with storms in tropics and Northern Hemisphere*, Geophys. Res. Lett., 33 (2006).

[19] P. A. Martin and L. Farina, *Radiation of water waves by a heaving submerged horizontal disc*, J. Fluid Mech., 337 (1997), pp. 365–379.

[20] R. A. Massom, T. A. Scambos, L. G. Bennetts, P. Reid, V. A. Squire, and S. E. Stammerjohn, *Antarctic ice shelf disintegration triggered by sea ice loss and ocean swell*, Nature, 558 (2018), pp. 383–389.

[21] P. McIver, *Complex resonances in the water-wave problem for a floating structure*, J. Fluid Mech., 536 (2005), pp. 423–443.

[22] P. McIver and R. Porter, *The motion of a freely floating cylinder in the presence of a wall and the approximation of resonances*, J. Fluid Mech., 795 (2016), pp. 581–610.

[23] M. H. Meylan, L. G. Bennetts, R. J. Hosking, and E. Catt, *On the calculation of normal modes of a coupled ice-shelf/sub-ice-shelf cavity system*, J. Glaciol., 63 (2017), pp. 751–754.

[24] M. H. Meylan and C. Fitzgerald, *Computation of long lived resonant modes and the poles of the S-matrix in water wave scattering*, J. Fluids Struct., 76 (2018), pp. 153–165.

[25] M. H. Meylan and C. J. Fitzgerald, *The singularity expansion method and near-trapping of linear water waves*, J. Fluid Mech., 755 (2014), pp. 230–250.

[26] M. H. Meylan, M.-u. Hassan, and A. Bashir, *Extraordinary acoustic transmission, symmetry, Blaschke products and resonators*, Wave Motion, 74 (2017), pp. 105–123.

[27] M. H. Meylan, M. Ilyas, B. Lamichhane, and L. G. Bennetts, *Swell induced vibrations of a thickening ice shelf over a shoaling seabed*, 2021, https://arxiv.org/abs/2103.05192.

[28] M. H. Meylan and M. Tomic, *Complex resonances and the approximation of wave forcing for floating elastic bodies*, Appl. Ocean Res., 36 (2012), pp. 51–59.

[29] A. Ooi, A. Nikolovska, and R. Manasseh, *Analysis of time delay effects on a linear bubble chain system*, J. Acoust. Soc. Am., 124 (2008), pp. 815–826.

[30] T. K. Papathanasiou, A. E. Karperaki, and K. A. Belibassakis, *On the resonant hydroelastic behaviour of ice shelves*, Ocean Model., 133 (2019), pp. 11–26.

[31] T. K. Papathanasiou, A. E. Karperaki, E. E. Theotokoglou, and K. A. Belibassakis, *Hydroelastic analysis of ice shelves under long wave excitation*, Nat. Hazard Earth Sys., 15 (2015), pp. 1851–1857.

[32] S. Rupprecht, L. G. Bennetts, and M. A. Peter, *Effective wave propagation along a rough thin-elastic beam*, Wave Motion, 70 (2017), pp. 3–14.

[33] O. V. Sergienko, *Normal modes of a coupled ice-shelf/sub-ice-shelf cavity system*, J. Glaciol., 59 (2013), pp. 76–80.

[34] O. V. Sergienko, *Behavior of flexural gravity waves on ice shelves: Application to the Ross Ice Shelf*, J. Geophys. Res.: Oceans, (2017).

[35] G. L. Vaughan, L. G. Bennetts, and V. A. Squire, *The decay of flexural-gravity waves in long sea ice transects*, Proc. Roy. Soc. A, 465 (2009), pp. 2785–2812.

[36] E. Wegert, *Visual Complex Functions: An Introduction with Phase Portraits*, Springer Science & Business Media, 2012.